Electrical Power and Energy Systems 117 (2020) 105649

Contents lists available at ScienceDirect

Electrical Power and Energy Systems

journal homepage: www.elsevier.com/locate/ijepes

Probabilistic transient stability assessment of power system considering wind power uncertainties and correlations

Ziyuan Yue[a], Yanli Liu[a,*], Yixin Yu[a], Junbo Zhao[b]

[a] Key Laboratory of Smart Grid of Ministry of Education, Tianjin University, Tianjin 300072, China
[b] Department of Electrical and Computer Engineering, Mississippi State University, Starkville, MS, 39759 USA

ARTICLE INFO

Keywords:
Cornish-Fisher expansion
Dynamic security region
Transient stability criterion
Three-point estimation
Wind farm correlation

ABSTRACT

This paper proposes a simple yet effective method for power system probabilistic transient stability assessment considering the wind farm uncertainties and correlations. Specifically, the inverse Nataf transformation based three-point estimation method and the Cornish-Fisher expansion have been integrated together to deal with the uncertainties and the correlations among different wind farms. Then, by resorting to the extended dynamic security region approach, the transient stability criterion is derived as a linear combination of nodal injection vector under a given fault condition. New indices for the identification of critical lines have also been developed. Extensive simulation results carried out on four different systems, including the practical GZ power system in China show that the computational efficiency of the proposed method is much higher than the Monte Carlo-based method and other methods almost without the loss of accuracy. The effectiveness of the proposed method under different penetrations of wind power with different degree of correlations is also validated. It is shown that correlation among wind farms has a larger impact on the transient stability results with a higher penetration level of renewable energy.

1. Introduction

Ever-increasing renewable energy represented by wind power has been integrated into the power system in recent years [1,2]. Unlike the traditional generation, the power output of the wind turbine is related to wind speed, which is uncertain and correlated [3]. In this context, the large-scale integration of wind power has a great impact on the transient stability of the power system [4–7]. From the perspective of planning and operation of power systems, an effective method for transient stability assessment considering the wind farm uncertainties and correlations has been becoming more and more important.

The widely used approach for transient stability assessment is deterministic. It uses the time-domain simulation to estimate whether the system is stable under the given fault and operating point. The results from the deterministic approach are typically conservative and even inaccurate if the uncertainties of wind power are neglected [8]. To deal with that, the complementary probabilistic approach is proposed, which can provide more insightful information about the system for operators and planners [9–11].

The probabilistic approach mainly includes two categories: the Monte Carlo (MC) simulation-based and the analytical approaches. For the MC simulation-based approach [12–16], a great number of sampling points are generated according to the probabilistic distribution of uncertain factors. The transient stability of each sampling point is analyzed by the time-domain simulation. The transient stability probability (TSP) is finally obtained according to the Law of Large Numbers. The MC simulation is applicable to various scenarios, including the uncertain and correlated wind power [13,14]. The larger the number of sampling points is, the higher the calculation accuracy is. However, the computing burden is very heavy. As a result, MC simulation is usually used as the reference method. Although the computational efficiency of it can be improved [14], it is not suitable for large-scale system online applications.

For the analytical approaches [17–25], the expressions of the probabilistic TSP indicators are derived. For example, after deriving the expression of the transient stability margin (TSM) [19], estimated the distribution of TSM with the Kalman filter and unscented transformation considering the wind power uncertainties. In [21], the normalized transient energy function and the bisection algorithm were used together to calculate the critical clearing time (CCT). Then the transient instability probability was obtained by establishing the expression between the probability index and the CCT to each given fault. However, the correlations of wind power are neglected which may deteriorate the performance of the TSP results. To deal with that, representative

* Corresponding author at: Key Laboratory of Smart Grid of Ministry of Education, Tianjin University, Tianjin 300072, China.
E-mail addresses: ziyuanyue@tju.edu.cn (Z. Yue), yanliliu@tju.edu.cn (Y. Liu), yixinyu@tju.edu.cn (Y. Yu), junbo@ece.msstate.edu (J. Zhao).

https://doi.org/10.1016/j.ijepes.2019.105649
Received 8 September 2019; Received in revised form 22 October 2019; Accepted 23 October 2019
Available online 15 November 2019
0142-0615/

sampling strategies, such as point estimation [24] and sample reduction method [25], to characterize the correlations of wind power are proposed when assessing the system transient stability. Due to the stochasticity and randomness of wind power, the derivations of analytical expressions are challenging. Furthermore, the time-consuming MC simulation is usually utilized to obtain the probabilistic index, which imposes difficulties in online applications.

To solve these issues, the security region approaches are proposed in our previous work [26,27]. They provide a powerful analytical tool for stability and security assessment [28–30]. Interestingly, it was found that the boundary of a practical dynamic security region with double fed induction generators (DFIGs) can be approximated by one or several hyper-planes [29]. As a result, the transient stability criterion can be expressed as a linear combination of nodal power injection vectors. Leveraging the concept of dynamic security region defined in the nodal power injection space of the pre-fault phase, an analytical expression of TSP can be established [30]. This paper further extends our previous work and presents a new probabilistic transient stability assessment approach considering wind power uncertainties and correlations. It has the following contributions:

- The concept of security region is extended to derive the analytical expression of probabilistic transient stability assessment index considering both wind farm uncertainties and correlations; the latter are not fully considered and only one wind farm is considered in our previous work [30]. While in this paper, multiple wind farms are tested with varying correlation coefficients, including both negative and positive correlations;
- We have integrated three-point estimation method with the inverse Nataf transformation to derive the analytical TSP index. New indices for the identification of critical lines have also been developed. This allows us to develop corresponding mitigation plans;
- Comprehensive tests have been carried out on four different systems, including practical GZ power system in China. This enables us to draw more generalized conclusions. In particular, the computational efficiency of the proposed method is much higher than the MC-based method and [25] with less than 5% deviation from the accurate results by MC-simulation.

The remainder of the paper is organized as follows. Section 2 presents the stochastic model of nodal power injection. Section 3 shows the proposed TSP assessment framework and the details of calculating the proposed TSP index. Section 4 shows and analyzes the simulation results and finally, Section 5 concludes the paper.

2. Stochastic model of nodal power injection

Three types of nodal injections are considered in the power system with DFIGs, including traditional generators, loads and DFIGs. Nodal injections from traditional generators and loads can be assumed to follow normal distributions $P_i = N(\mu_i, \sigma_i^2)$, where μ_i is the mean. For the load, μ_i is usually obtained from the load forecasting [30] while it is set to be the nominal value for the traditional generator. σ_i is the standard deviation that can be obtained from the historical data [31,32].

The output power of the DFIG is related to wind speed, the distribution of which is modeled as Weibull distribution [33,34]. Its probability density function (PDF) is shown in (1):

$$f(v) = (k/c)(v/c)^{k-1}\exp[-(v/c)^k] \tag{1}$$

where k and c are the Weibull shape scale parameters, respectively. They can be calculated via (2) and (3):

$$k = (\sigma/\mu)^{-1.086} \tag{2}$$

$$c = \mu/\Gamma(1 + 1/k) \tag{3}$$

where μ and σ are the mean and the standard deviation of wind speed respectively; Γ is the Gamma function.

Then the active power of DFIG is given as [35]:

$$P_w = \begin{cases} 0 & v < v_{ci} \text{ or } v > v_{co} \\ P_r \frac{v^3 - v_{ci}^3}{v_r^3 - v_{ci}^3} & v_{ci} \leqslant v \leqslant v_r \\ P_r & v_r < v \leqslant v_{co} \end{cases} \tag{4}$$

where P_r is the rated capacity of DFIG; P_w is the actual active power of DFIG. v_{ci}, v_{co}, and v_r are the cut-in, cut-out, and rated wind speeds, respectively.

The PDF of the DFIG real power is expressed as follows by using (1) and (4):

$$f(P_w) = (k'/c')((P_w - \gamma')/c')^{k'-1} \times \exp(-((P_w - \gamma')/c')^{k'}) \tag{5}$$

where c', k', and γ' are given in (6), (7), and (8) [36]:

$$c' = P_r c^3/(v_r^3 - v_{ci}^3) \tag{6}$$

$$k' = k/3 \tag{7}$$

$$\gamma' = -P_r v_{ci}^3/(v_r^3 - v_{ci}^3) \tag{8}$$

In practice, an aggregated wind farm model is used to represent a group of DFIGs. The mean is taken from the wind power forecast and the standard deviation is set as 20% of the mean value [37].

3. Proposed TSP assessment framework

TSP is a probabilistic indicator to analyze the transient stability of the system. In this paper, the security region is extended to derive the analytical expression of probabilistic transient stability assessment index considering both wind farm uncertainties and correlations.

3.1. Boundary of dynamic security region with DFIG

Given a specific fault, the power system will experience three phases, namely the pre-fault, fault-on, and post-fault phases. Their corresponding state equations are given as:

$$\dot{\mathbf{x}} = \begin{cases} \mathbf{f}_i(\mathbf{x}) & -\infty < t < 0 \\ \mathbf{f}_F(\mathbf{x}) & 0 \leqslant t < \tau \\ \mathbf{f}_j(\mathbf{x}) & \tau \leqslant t < +\infty \end{cases} \tag{9}$$

where x is the state vector at different phases; τ is the duration time of the fault; i, F, j represent configuration of pre-fault, fault-on and post-fault, respectively; $\boldsymbol{f}$ is the corresponding state equation.

Define the dynamic security region for the system transition from configuration i to configuration j as the result of a fault clearing in τ sec., $\Omega_d(i, j, F)$ to be the set of pre-fault injections $\boldsymbol{y}$ for which the system is transient stable. A system is said to be transient stable if the post-fault system trajectory will settle down to a stable post-fault equilibrium point, the solution of which depends on the pre-fault injection $\boldsymbol{y}$. Consequently, let A denote the set of post-fault initial states for which the system is transient stable and the region A is a function of $\boldsymbol{y}$. $A(\boldsymbol{y})$ is the transient stability region in the state space, which surrounds the stable equilibrium point of post-fault phase corresponding to $\boldsymbol{y}$. $x_d(\boldsymbol{y})$ is used to represent the state variables after the fault is cleared. $\Omega_d(i, j, F)$ is the set of injections $\boldsymbol{y}$ for which $x_d(\boldsymbol{y})$ lies in $A(\boldsymbol{y})$, i.e.,

$$\Omega_d(i, j, F) = \{y \mid x_d(y) \in A(y)\} \tag{10}$$

The relationship between $\Omega_d(i, j, F)$ and $A(\boldsymbol{y})$ is further shown in Fig. 1.

In the scope of engineers' concern, the practical dynamic security region (PDSR) of power system with DFIG can be approximated by one or few hyper-planes [27–29]:

$$\sum_{i=1}^{n} \alpha_i P_i + \beta_i Q_i = 1 \tag{11}$$

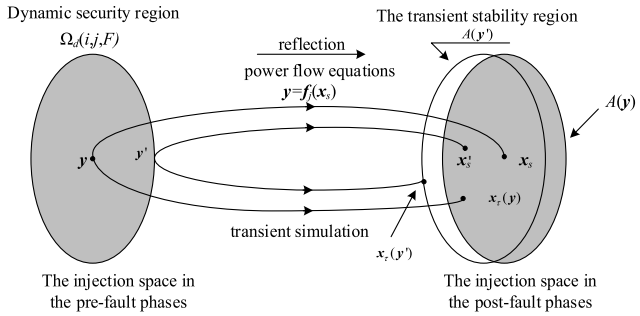

Fig. 1. The relationship between $\Omega_d(i, j, F)$ and $A(\boldsymbol{y})$.

where n is the number of nodes; α_i, β_i are the coefficients of the hyper-plane equation related to node i; P_i and Q_i represent critical active and reactive power injection at node i, respectively, in the space of pre-fault power injection to guarantee transient stability. This paper mainly focuses on the rotor angle stability and it is assumed that the local reactive power reserve is sufficient to maintain the voltage stability [38]. Thus, the dynamic security region [39] can be represented via:

$$\sum_{i=1}^{n} \alpha_i P_i = 1 \tag{12}$$

The dynamic security region is unique to a given fault. Substituting active power injections into the left side of (12), the system is transient stable when the value is less than 1 and vice versa. The dynamic security region provides an effective way to simplify the relationship between power injection and transient stability criterion. Interested readers can find more details about PDSR from [27–30].

3.2. Proposed TSP index

The TSP represents the probability of transient stability of the system. Considering uncertainties of nodal power injection and no simple mathematical description about Ω_d, TSP is an extraordinary complicated n-degree integral in n-dimension power injection space shown as follows:

$$\mathrm{TSP} = \iint \cdots_{y\in\Omega d} \int f(y_1, y_2, \cdots, y_n) dy_1 dy_2 \cdots dy_n \tag{13}$$

where $\boldsymbol{y}$ is the vector of random variables of injection power; f is the probability density function of $\boldsymbol{y} = (y_1, y_2, \ldots, y_n)^{\mathrm{T}}$.

Based on PDSR expressed by (12), the (13) can be converted to a much simpler analytical calculation shown as follows:

$$\mathrm{TSP} = \Pr\left\{\sum_{i=1}^{n} \alpha_i P_i \leqslant 1\right\} = G(S)|_{s=0} \tag{14}$$

where $S = \sum_{i=1}^{n} \alpha_i P_i - 1$; n represents the nodes including the traditional generations, loads and wind farms; $G(S)$ is the cumulative distribution function (CDF) of S; α_i are the coefficients of the hyper-plane equation related to node i and P_i is the active injection at the i node.

3.3. Calculate proposed TSP index

The key to calculate TSP is to obtain $G(S)$ considering the correlations of wind farms. Point estimation method (PEM) is a powerful yet simple approximation method used to evaluate the first few moments of a function of random variables. It only relies on a few discrete points which are determined by the Taylor expansion. However, the PEM is based on the assumption that the random variables are independent, which can't deal with the correlation among wind farms. Therefore, the PEM is improved by introducing the inverse Nataf transformation [40] by transforming the uncorrelated standard normal distribution variables into the original correlated variables. Once the moments of dependent variable are calculated, the distribution of dependent variable can be obtained by Cornish-Fisher expansion. The proposed method contains four main steps: (1) three-point estimation to approximate the distributions of original state variables without correlations; (2) inverse Nataf transformation to modify the sample points from three-point estimation so that correlations among state variables are effectively taken into account; (3) calculation of index S via the generated sample points; (4) evaluation of the stability index by the Cornish-Fisher expansion. The detailed steps are shown as follows:

Step 1: Calculate 2n + 1 uncorrelated normal distribution evaluation vectors and their corresponding weights

Each uncorrelated normal distribution variable $x_i = N(0,1)$, (i = 1, 2, ··, n) has three locations $x_{i,k}$ (k = 1, 2, 3), which are calculated as:

$$x_{i,k} = \mu_{x_{i,k}} + \varepsilon_{x_{i,k}} \sigma_{x_i} \quad k = 1, 2, 3 \tag{15}$$

where i = 1, 2, …, n; $\varepsilon_{x_{i,k}}$, $\mu_{x_{i,k}}$, and $\sigma_{x_{i,k}}$are the standard location, the mean and standard deviation of x_i, respectively.

The standard locations, $\varepsilon_{x_{i,k}}$ are given by:

$$\begin{cases} \varepsilon_{x_{i,k}} = \lambda_{x_i}/2 + (-1)^{3-k} \times \sqrt{\nu_{x_i} - 3/4\lambda_{x_i}^2} & k = 1, 2 \\ \varepsilon_{x_{i,3}} = 0 \end{cases} \tag{16}$$

where λ_{x_i} and ν_{x_i} are respectively the skewness and the kurtosis of the variable, x_i. If x_i are normal distributions, λ_{x_i} and ν_{x_i} are set to be 0 and 3, respectively.

Each location $x_{i,k}$ is coupled with a weight$\omega_{x_{i,k}}$:

$$\begin{cases} \omega_{x_{i,k}} = (-1)^{3-k}/(\varepsilon_{x_{i,k}}(\varepsilon_{x_{i,1}} - \varepsilon_{x_{i,2}})) \\ \omega_{x_{i,3}} = 1/n - 1/(\nu_{x_i} - \lambda_{x_i}^2) \end{cases} \tag{17}$$

where n is the number of input random variables.

As a result, each evaluation vector is represented by

$$\begin{aligned} X_{i,k} &= [\mu_{x_1}, \mu_{x_2}, \cdots, \mu_{x_{i-1}}, x_{i,k}, \mu_{x_{i+1}} \mu_{x_{i+2}} \mu_{x_n}] \\ &= [0, \cdots, 0, x_{i,k}, 0, \cdots, 0] \end{aligned} \tag{18}$$

It can be seen that 3n evaluations are needed. While, since $\varepsilon_{x_{i,3}} = 0$ is valid for all random input variables, there are n evaluation vectors shown as $\boldsymbol{X}$ = [0, …, 0, 0, 0, …, 0]. Therefore, only 2n + 1 evaluations need to be performed in implementation with the corresponding weights $\omega_{x_{1,1}}$, $\omega_{x_{1,2}}$, $\cdots$,$\omega_{x_{n,1}}$, $\omega_{x_{n,2}}$, $\omega_{x_{2n+1}}$.

Step 2: Calculate 2n + 1 evaluation vectors and their weights in the original space

Let $\boldsymbol{P}_i$ (i = 1, 2, …, n) represent the nodal active power injections in the original space, including the traditional generators, loads and DFIGs and z_i (i = 1, 2, …, n) represent the correlated standard normal distribution variables. If the correlation matrices of $\boldsymbol{z}$ and $\boldsymbol{P}$ are ρ_0 and ρ, respectively, the expression between them can be expressed as follows according to the Nataf transformation:

$$\begin{aligned} \rho_{ij} &= \int_{-\infty}^{+\infty} \int_{-\infty}^{+\infty} (P_i - \mu_i)/\sigma_i (P_j - \mu_j)/\sigma_j \\ &\quad f_{ij}(P_i, P_j) dP_i dP_j \\ &= \int_{-\infty}^{+\infty} \int_{-\infty}^{+\infty} (F_i^l(\Phi(z_i)) - \mu_i)/\sigma_i \\ &\quad (F_j^l(\Phi(z_j)) - \mu_j)/\sigma_j \\ &\quad \Phi(z_i, z_j, \rho_{0ij}) dz_i dz_j \end{aligned} \tag{19}$$

where μ_i and μ_j are the means of $\boldsymbol{P}_i$ and $\boldsymbol{P}_j$, respectively; σ_i and σ_j are the standard deviations of $\boldsymbol{P}_i$ and $\boldsymbol{P}_j$, respectively; $\Phi(z_i, z_j, \rho_{0ij})$ is the joint probability distribution of z_i and z_j.

To simplify the analysis, ρ_{0ij} is calculated by the semi-empirical formula in [31]. Since ρ_0 is a positive definite symmetric matrix, it can be decomposed into lower triangular matrix $\boldsymbol{B}$ by Cholesky decomposition:

$$\rho_0 = BB^T \tag{20}$$

Then, the 2n + 1 evaluation vectors $\boldsymbol{X}_{i,k}$ are transformed into the evaluation vectors $\boldsymbol{Z}_{i,k}$ via (21):

$$Z = BX \tag{21}$$

Then, the elements of each evaluation vector in the original space are transformed by:

$$P_i = F^{-1}(\Phi(z_i)) \tag{22}$$

where $F^{-1}(\cdot)$ represents the inverse CDF of the nodal active power injections. After that, the $2n + 1$ evaluation vectors $\boldsymbol{Z}_{i,k}$ can be transformed into the original space, namely $P_{1,1}$, $P_{1,2}$, …, $P_{n,1}$, $P_{n,2}$, P_{2n+1}.

Finally, the process that transforms $\boldsymbol{X}_{i,k}$ to $\boldsymbol{P}_{i,k}$ is the inverse Nataf transformation. The weights corresponding to evaluation vectors are $\omega_{x_{1,1}}$, $\omega_{x_{1,2}}$, $\cdots$,$\omega_{x_{n,1}}$, $\omega_{x_{n,2}}$, $\omega_{x_{2n+1}}$.

Step 3: Get the raw moments of S based on evaluation vectors and weights in the original space

According to (14), S is expressed as follows:

$$S = \sum_{i=1}^{n} \alpha_i P_i - 1 = H(P_1, P_2, \cdots, P_n) \tag{23}$$

where H is the nonlinear function; P_i represents the active power injection of node i in the original space. $2n + 1$ evaluations are obtained by substituting each evaluation vector into (23), yielding $C_{1,1}$, $C_{1,2}$, …, $C_{n,1}$, $C_{n,2}$, C_{2n+1} and weights, $\omega_{x_{1,1}}$, $\omega_{x_{1,2}}$, $\cdots$,$\omega_{x_{n,1}}$, $\omega_{x_{n,2}}$, $\omega_{x_{2n+1}}$, respectively. Then, the l-order raw moment of S is as follow:

$$E(S^l) \approx \sum_{i=1}^{n} \sum_{k=1}^{2} \omega_{x_{i,k}} C_{i,k}^l + \omega_{x_{2n+1}} C_{2n+1}^l \tag{24}$$

Step 4: Obtain TSP by the Cornish-Fisher expansion

The Cornish-Fisher expansion provides an approximation of a quantile α of a distribution function $F(y)$ in terms of the quantile of a standard normal distribution Φ and the cumulants of $F(y)$. In particular, $y(\alpha)$ can be expressed as:

$$\begin{aligned} y(\alpha) \cong\ & \xi(\alpha) + (\xi^2(\alpha) - 1)/6g_3 + \\ & (\xi^3(\alpha) - 3\xi(\alpha))/24g_4 - \\ & (2\xi^3(\alpha) - 5\xi(\alpha))/36g_3^2 + \\ & (\xi^4(\alpha) - 6\xi^2(\alpha) + 3)/120g_5 + \cdots \end{aligned} \tag{25}$$

where $\xi(\alpha) = \Phi^{-1}(\alpha)$; g_v is the normalized v-order of cumulant. The latter can be calculated using (26) and (27).

The first three cumulants of S are:

$$\begin{cases} K_1 = E(S) \\ K_2 = E(S^2) - K_1^2 \\ K_3 = E(S) - 3K_1K_2 - K_1^3 \end{cases} \tag{26}$$

where $E(S^l)$ is the l-order raw moment of S.

Then, the normalized v-order of cumulants are as follow:

$$g_v = K_v/\sigma^v = K_v/K_2^{v/2} \tag{27}$$

Finally, $G(S)$ is obtained according to $y(\alpha) = F^{-1}(\alpha)$ and the TSP is calculated via (14).

4. Numerical results

4.1. Effectiveness of the proposed method

4.1.1. IEEE 39-bus system

The effectiveness of the proposed approach is first validated on IEEE 39-bus system, whose diagram is shown in Fig. 2. The traditional generators at nodes 33 and 34 are replaced by two wind farms with the capacities, 632 MW and 508 MW, respectively. Cut-in, cut-out, and rated wind speed are set to be 4 m/s, 23 m/s, and 15 m/s, respectively. The $N - 1$ faults listed in Table 1 are considered. The fault type is three-phase short circuit fault and the clearing time is 0.1 s. The coefficients of hyper-planes for the dynamic security region corresponding to each fault can be found in [30]. Five cases considering positive and negative correlation coefficients (CCs) [41] are tested as shown in Table 2. The Weibull parameters $k = 5.742$, the scale parameters, c, are 313.26, 251.80 and γ are -0.1222, -0.0982 for the wind farms at nodes 33 and 34, respectively.

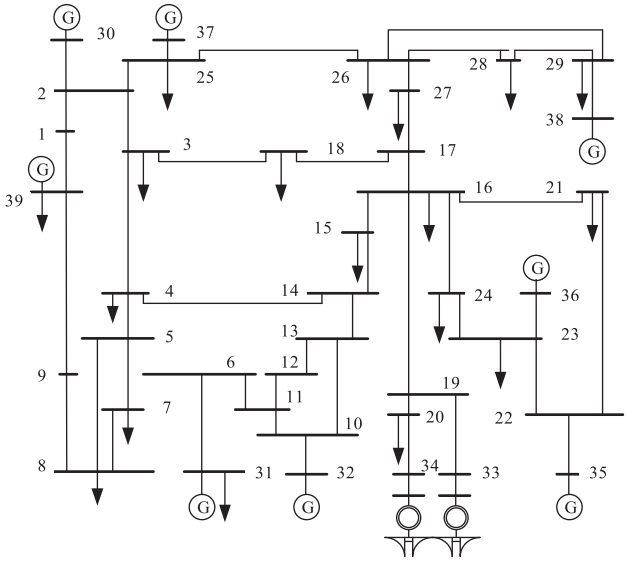

Fig. 2. IEEE 39-bus System with two wind farms.

Table 1
Fault line list.

Number	Fault line	Number	Fault line	Number	Fault line
1	1–2	13	7–8	25	17–18
2	1–39	14	8–9	26	17–27
3	2–3	15	9–39	27	21–22
4	2–25	16	10–11	28	22–23
5	3–4	17	10–13	29	23–24
6	3–18	18	13–14	30	25–26
7	4–5	19	14–15	31	26–27
8	4–14	20	15–16	32	26–28
9	5–6	21	16–17	33	26–29
10	5–8	22	16–19	34	28–29
11	6–7	23	16–21		
12	6–11	24	16–24		

Table 2
Cases C1-C5 corresponding to different CCs.

Case	CC among the wind farms
Case C1	0
Case C2	0.5
Case C3	0.8
Case C4	−0.5
Case C5	−0.8

The TSP results by MC simulation method with 50,000 samples is treated as the reference and (14) is taken as the stability index for each sample. The TSP results provided by the proposed method and MC considering positive and negative CCs are displayed in Figs. 3 and 4, respectively, in which the lines with TSP $<$ 0.995 are shown. For Case C3, the $G(S)$ provided by the proposed method and the MC simulation corresponding to the fault lines 2–3 and 2–25 are shown in Figs. 5 and 6. The computing time of both the proposed method and MC simulation for all five cases are presented in Table 3.

From the results shown in Figs. 3–6 and Table 3, it can be concluded that the proposed method is able to achieve comparable accuracy as the

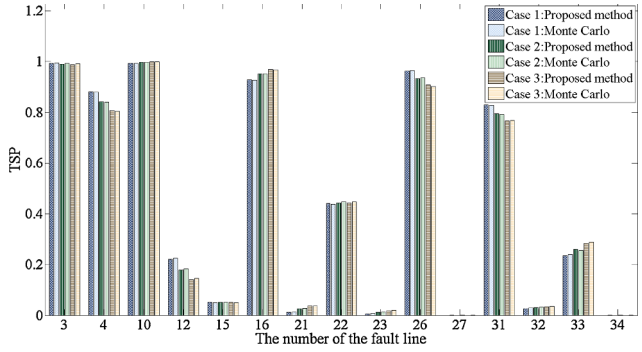

Fig. 3. TSP by the proposed method and MC for Cases C1-C3 on IEEE 39-bus system.

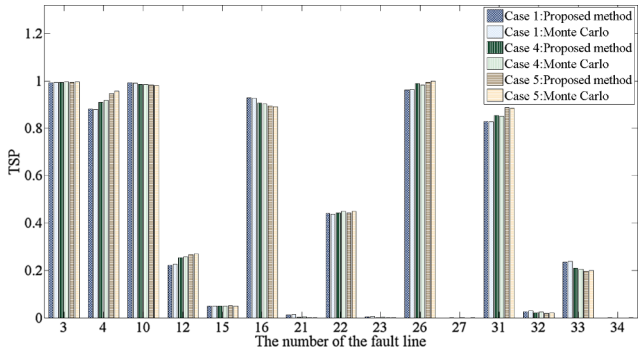

Fig. 4. TSP by the proposed method and MC for Cases C1, C4 and C5 on IEEE 39-bus system.

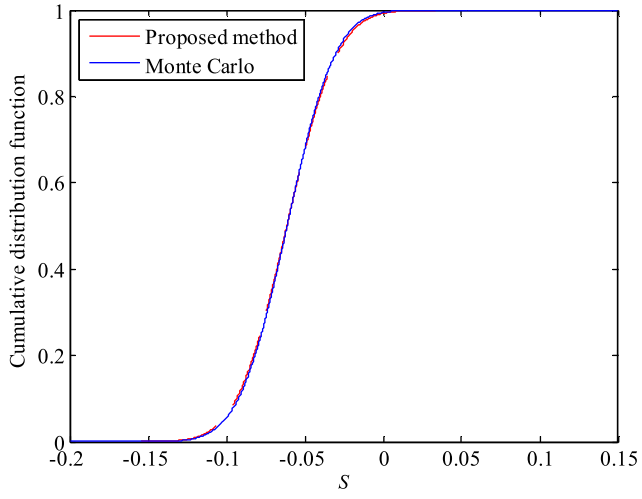

Fig. 5. $G(S)$ by the proposed method and MC for fault line 2–3.

MC method while maintaining much higher computational efficiency. Comparing with MC, the largest error of the TSP for all N-1 faults are 2.32%, 3.78%, 2.85%, 2.03%, and 1.71% in five cases, respectively.

Considering the maximum wind penetration level is 40%, the proposed method is further tested in another two cases W1-W2 corresponding to different number of wind farms as shown in Table 4. The computing times of the proposed method and MC for Cases W1-W2 are shown in Table 5. Compared with MC, the largest error and average error for all N-1 faults under different CCs are provided in Table 6. It can be further concluded that with varying number of wind farms under different CCs, the proposed method can still get accurate TSP results with much faster computing speed than the MC method.

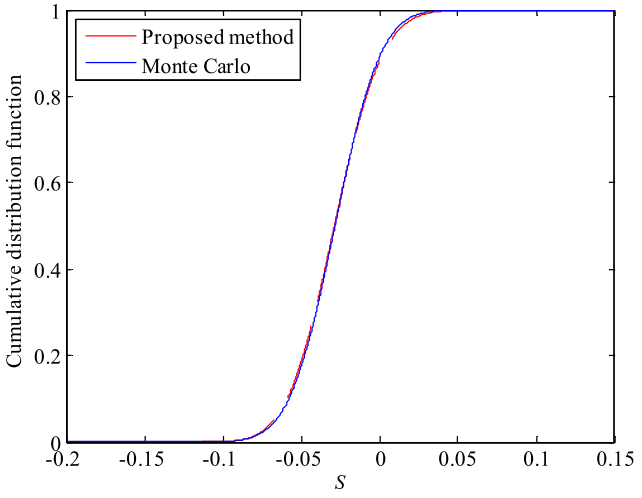

Fig. 6. $G(S)$ by the proposed method and MC for fault line 2–25.

Table 3
Computing time of the proposed method and MC on IEEE 39-bus system.

Case	Proposed method	MC
Case C1	1.45 s	139.73 s
Case C2	1.67 s	126.71 s
Case C3	1.56 s	154.72 s
Case C4	1.76 s	141.02 s
Case C5	1.66 s	133.58 s

Table 4
Cases W1-W2 corresponding to different number of wind farms.

Case	Number of wind farms	Installation locations
Case W1	3	33,34,35
Case W2	4	32,33,34,35

Table 5
Computing time of proposed method and MC for W1-W2.

Case	Proposed method	MC
Case W1	1.31 s	153.24 s
Case W2	1.53 s	150.44 s

Table 6
Errors of proposed method for cases W1-W2.

Case	Average error (%)					Largest error (%)
	C1	C2	C3	C4	C5	
W1	0.48	0.30	0.45	0.30	0.25	6.05
W2	0.13	0.25	0.19	0.20	0.18	2.86

4.1.2. Practical system in China and other IEEE systems

A practical provincial grid in China, i.e. GZ power system, is further used to test the proposed method. It includes 3080 buses and 3615 branches. Two large wind farms are installed in the nodes, GPTg1 and SLg4, with the capacities 460 MW and 260 MW, respectively. Three critical N-1 faults according to practical operation experience are considered, i.e. the ST, TS and FS lines. TSPs corresponding to different CCs among wind farms provided by the proposed method and MC are displayed in Fig. 7. The computing times and largest estimation error of the proposed method are shown in Table 7. More test results on IEEE

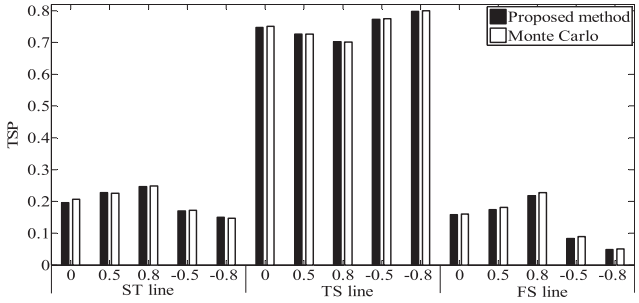

Fig. 7. TSP by proposed method and MC with different CCs on GZ system.

Table 7
Computing time and calculation errors of proposed method on GZ system.

	Computing time (s)		Largest error (%)
	Proposed method	MC	
CC = 0	2.35	345.85	3.57
CC = 0.5	2.14	405.75	2.58
CC = 0.8	2.04	434.53	2.79
CC = -0.5	2.15	415.84	4.20
CC = -0.8	2.05	423.66	4.15

Table 8
Test results of three systems.

Test system	Node/capacity of wind farm	Computing time (s)/ largest error (%)	Time cost of MC (s)
118-bus System	59/155, 61/160	1.72/4.26	213.48
300-bus System	152/372, 153/216	2.11/4.53	240.05
GZ system	GPTg1/460, SLg4/ 260	2.51/4.60	435.05

Table 9
Settings of cases M1-M4.

Case	The number of wind farms	Installation location
Case M1	3	GPTg1-g2, SLg4
Case M2	4	GPTg1-g3, SLg4
Case M3	5	GPTg1-g4, SLg4
Case M4	6	GPTg1-g5, SLg4

Table 10
Computing time of two methods for cases M1-M4.

Case	Proposed method	MC
Case M1	2.48 s	395.21 s
Case M2	2.25 s	348.54 s
Case M3	2.15 s	364.15 s
Case M4	2.34 s	386.54 s

TABLE 11
Errors of proposed method for cases M1-M4.

Case	Average error (%)					Largest error (%)
	C1	C2	C3	C4	C5	
M1	1.83	1.31	2.77	2.06	3.49	4.89
M2	2.26	1.43	1.35	1.72	1.41	2.97
M3	2.86	1.34	3.04	1.21	1.42	4.93
M4	1.32	3.58	1.73	2.12	2.67	4.26

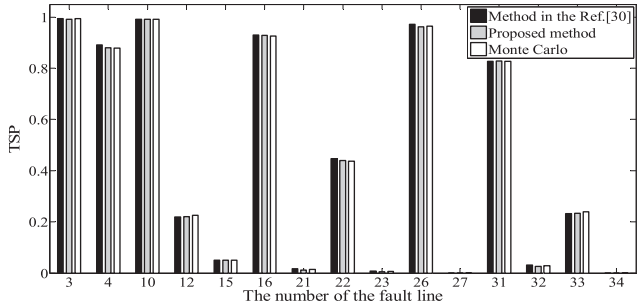

Fig. 8. Comparison among method in the Ref. [30], the proposed method and MC in Case C1 on IEEE 39-bus system.

118-bus and 300-bus systems are shown in Table 8.

Cases M1-M4 considering multiple wind farms in GZ system shown in Table 9 are also studied and the test results are displayed in Tables 10 and 11.

It can be observed from the above results that the proposed method is able to achieve comparable accuracy with the MC method but much less computing cost for large-scale systems with varying CC and number of wind farms.

4.2. Comparison with other methods

Some methods have been used for probabilistic transient stability assessment of power systems, i.e., the methods in [25] and [30]. The method from [30] is able to obtain TSP with high accuracy when the wind farms are without correlations in Case C1, see Figs. 8 and 9 for example. However, correlations usually exist among wind farms. Taking IEEE 39-bus system as an example, the average differences of TSP obtained by MC between Cases C1, C3 and Case C5 are 11.362% and 9.039%, respectively; the maximum differences are 36.634% and 27.465%, respectively. While for the GZ system, the average differences between Case C1 and Case C3, Case C5 are 28.65% and 32.13%, and the maximum differences are 49.01% and 67.97%, respectively. The comparison results of [30], the proposed method and MC in Case C3 and C5 on GZ power system are shown in Figs. 10 and 11. These results confirm that the proposed method can get much more accurate results than the method in [30] in the presence of wind power correlations.

By contrast, although the method in [25] is able to take into account the wind farm correlations, it has much higher computational burden than our proposed method. This can be demonstrated by the results shown in Tables 12 and 13, where the computing times of the proposed method and [25] by parallel computing for three different faults on two systems are tabulated.

4.3. Proposed TSP index vs deterministic stability margin

To provide more insights of the results, taking the case in Section 4.1.1 as an example, for the 1st, 12th, 27th, and 31st faults in Case C2, the operating points and the boundaries of PDSR in the space organized

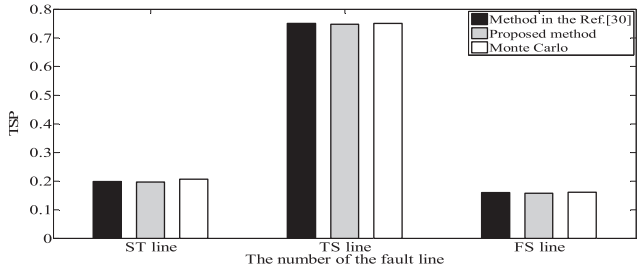

Fig. 9. Comparison among method in the Ref. [30], the proposed method and MC in Case C1 on GZ power system.

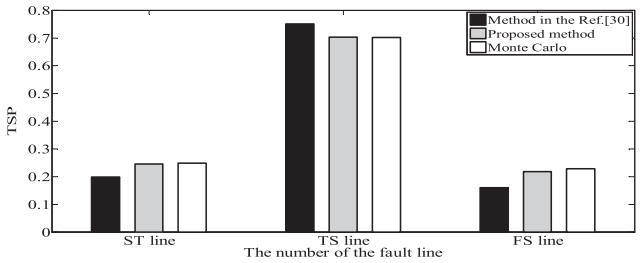

Fig. 10. Comparison among method in the Ref. [30], proposed method and MC in Case C3 on GZ power system.

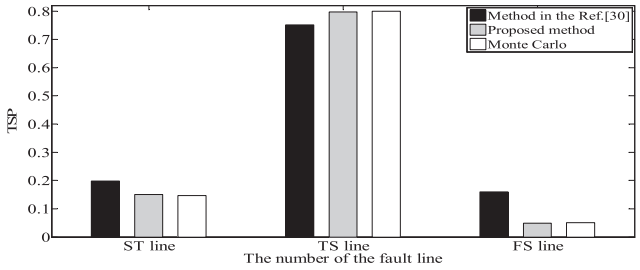

Fig. 11. Comparison among method in the Ref. [30], the proposed method and MC in Case C5 on GZ power system.

Table 12
Comparisons between the proposed method and [25] on IEEE 39-bus system.

Fault line	Proposed method	Method in [25]
1–2	1.47 s	92.45 s
6–11	1.82 s	91.36 s
10–11	1.62 s	92.97 s

Table 13
Comparisons between the proposed method and [25] on GZ power system.

Fault line	Proposed method	Method in [25]
ST line	2.55 s	173.65 s
TS line	2.37 s	172.49 s
FS line	2.46 s	176.35 s

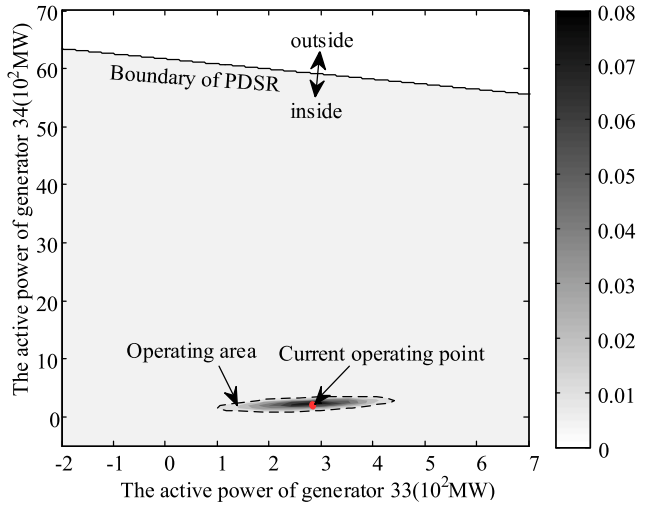

Fig. 12. PDSR boundary and the sampling point under the 1st fault in Case C2.

by the generators 33 and 34 are shown in Figs. 12–15, respectively, in which the gray and white represent the inside and outside of the boundary of PDSR, respectively. Note that the current operating point is

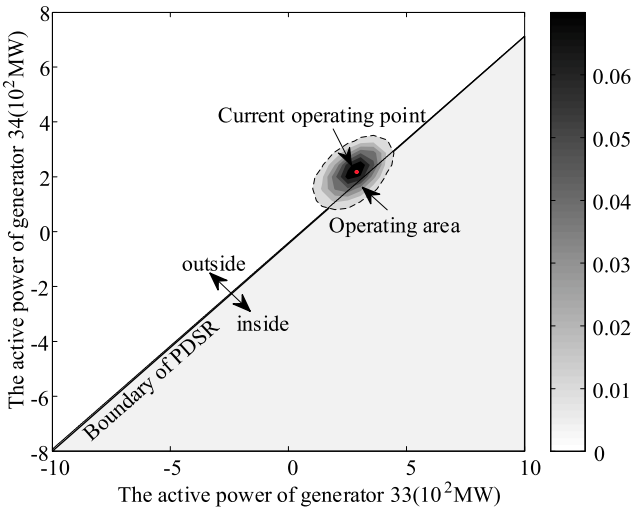

Fig. 13. PDSR boundary and the sampling points under the 12th fault in Case C2.

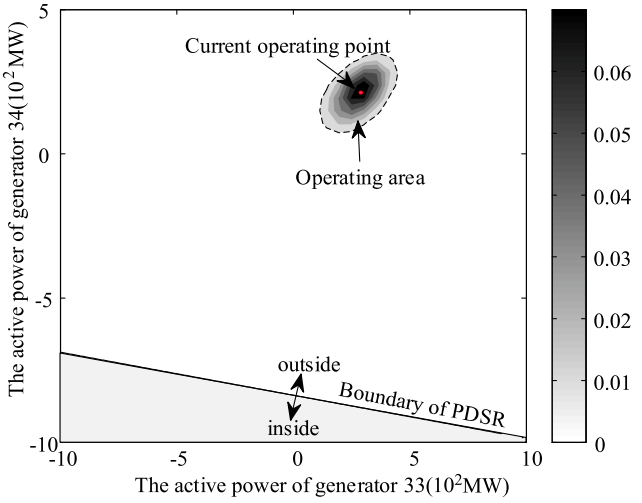

Fig. 14. PDSR boundary and the sampling points under the 27th fault in Case C2.

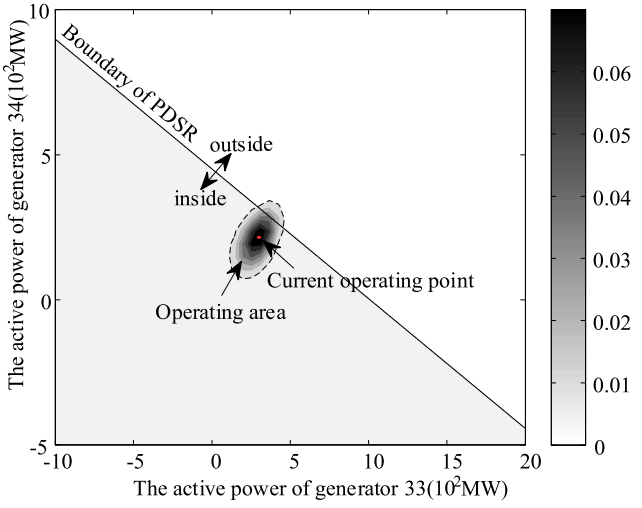

Fig. 15. PDSR boundary and the sampling points under the 31st fault in Case C2.

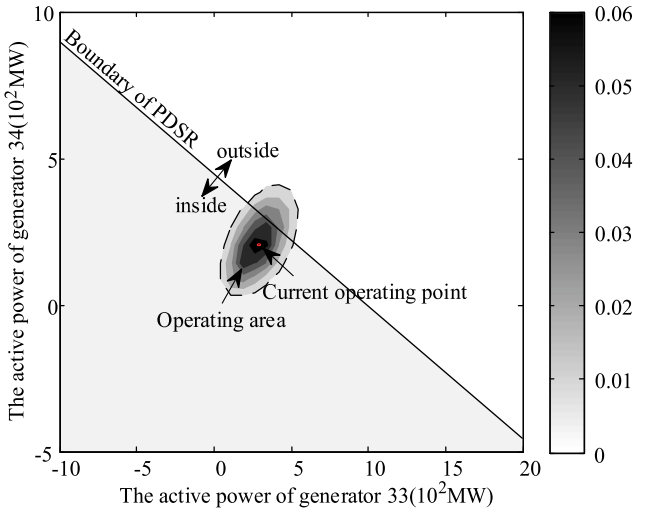

Fig. 16. PDSR boundary and the sampling points considering the 40% standard deviation of wind power under the 31st fault in Case C2.

Table 14
Cases P1-P6 Settings of Different Penetration Levels on IEEE 39-bus System.

Cases	Capacity of wind farm at the node 33 (MW)	Capacity of wind farm at the node 34 (MW)	Penetration level of wind power
Case P1	343.3	275.9	10%
Case P2	686.6	551.9	20%
Case P3	1029.9	827.7	30%
Case P4	1373.2	1103.6	40%
Case P5	1716.5	1379.5	50%
Case P6	2059.8	1655.4	60%

Table 15
Cases L1-L3 settings of different penetration levels on GZ power system.

Cases	Capacity of wind farm at the node GPTg1 (MW)	Capacity of wind farm at the node SLg4 (MW)
Case L1	230	130
Case L2	460	260
Case L3	690	390

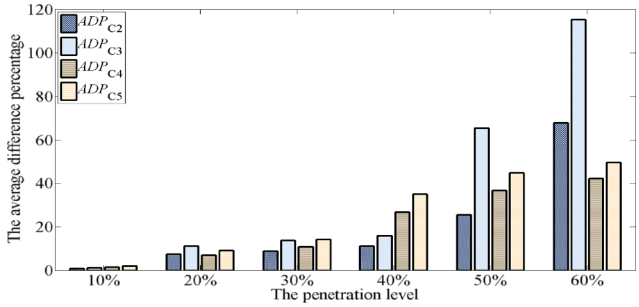

Fig. 17. Values of ADP_{C2}, ADP_{C3}, ADP_{C4}, and ADP_{C5} for Cases P1-P6.

represented as the red point. Considering the uncertainties of nodal injection power, the possible operating area is described by a number of points corresponding to different combinations of nodal injection power. In the operating area, the degree of the shadow color represents the density of the points.

For the current operating point, whether the system is transient stable or not can be evaluated by judging whether the operating point is inside the boundary of PDSR. As shown in Figs. 12–15, the system is transient stable, unstable, unstable and stable respectively if the uncertainties of the nodal injection power are neglected. By taking that

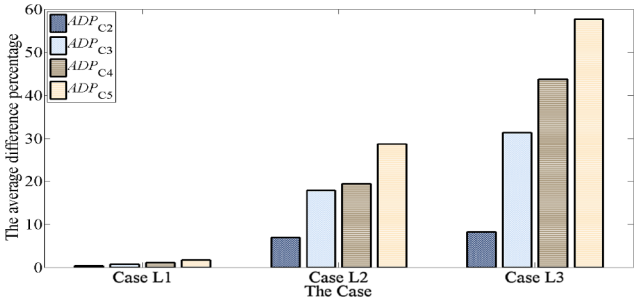

Fig. 18. Values of ADP_{C2}, ADP_{C3}, ADP_{C4}, and ADP_{C5} for Cases L1-L3.

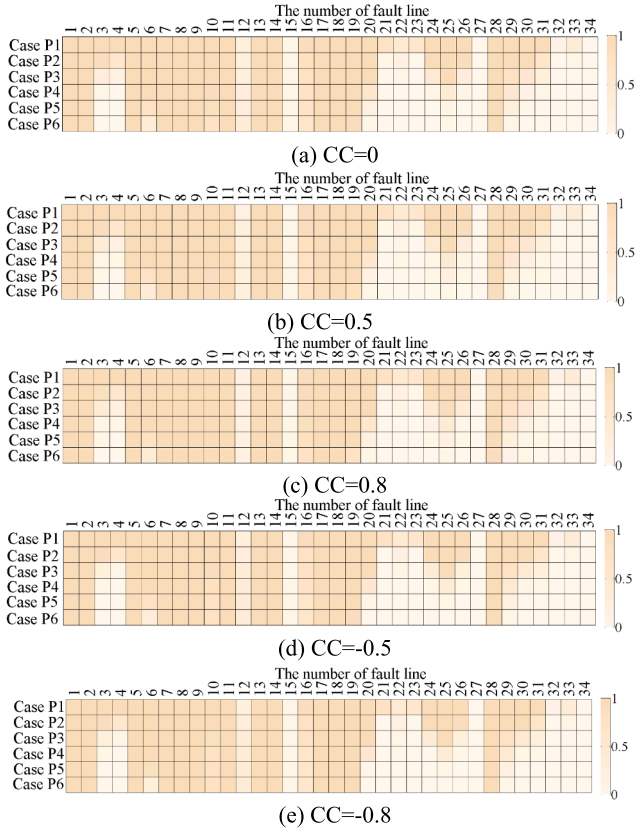

Fig. 19. TSP corresponding to each fault line in Cases P1-P6 with different CCs.

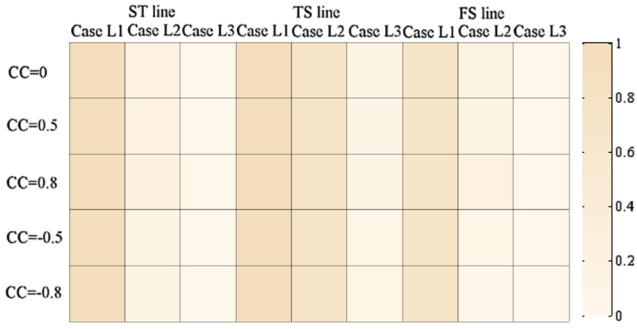

Fig. 20. TSP corresponding to each fault line for Cases L1-L3 with different CCs.

into account, TSP reflects the number of possible operating points inside the boundary. The larger TSP is, more stable the system is. From Figs. 12 and 14, the system is transient stable under the 1st fault and transient unstable under the 27th fault no matter the nodal injection powers change and the TSP are 1 and 0, respectively.

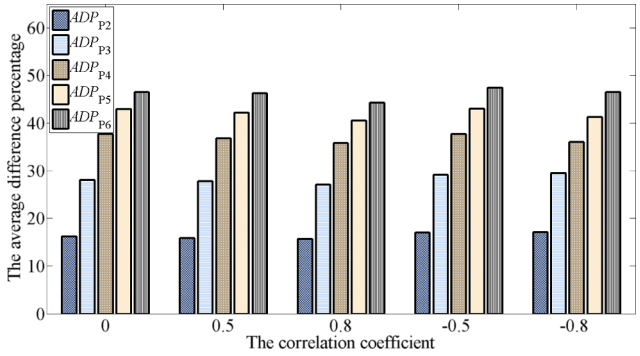

Fig. 21. Values of ADP_{P2}, ADP_{P3}, ADP_{P4}, ADP_{P5}, and ADP_{P6} for five CCs.

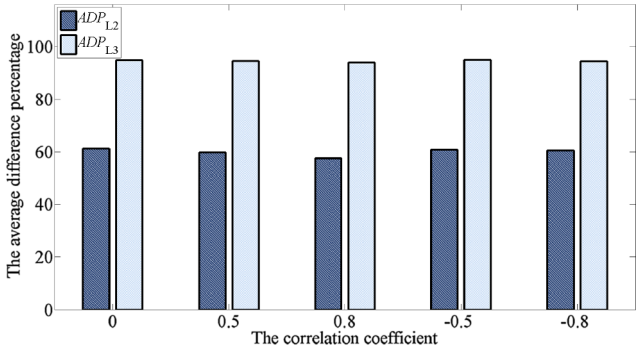

Fig. 22. Values of ADP_{L2} and ADP_{L3} for five CCs.

Table 16
Critical lines in cases P1-P6 with different CCs.

Case	cc = 0	cc = 0.5	cc = 0.8	cc = -0.5	cc = -0.8
P1	27, 34	27, 34	27, 34	27, 34	27, 34
P2	27, 34	27, 34	27, 34	27, 34	27, 34
P3	27, 34	27, 34	27, 34	27, 34	27, 34
P4	21, 23, 27, 32, 34	21, 23, 27, 32, 34	21, 23, 27, 32, 34	21, 23, 27, 32, 34	21, 23, 27, 32, 34
P5	21, 23, 27, 32, 34	21, 23, 27, 32, 34	21, 23, 27, 32, 34	21, 23, 27, 32, 34	21, 23, 27, 32, 34
P6	21, 23, 27, 32, 33, 34	21, 23, 27, 32, 33, 34	21, 23, 27, 32, 33, 34	21, 23, 27, 32, 33, 34	21, 23, 27, 32, 33, 34

Table 17
Most sensitive line to the CC.

	Case P1	Case P2	Case P3	Case P4	Case P5	Case P6
The number of fault line	12	12	12	12	12	12

Table 18
Most sensitive line to renewable energy penetration level.

	cc = 0	cc = 0.5	cc = 0.8	cc = -0.5	cc = -0.8
The number of fault line	23	23	23	23	23

It is interesting that for the results shown in Figs. 13 and 15, some operating points are inside the boundary while the others are outside. Specifically, the TSP value corresponding to the 31st fault is larger. From these results, it can be found that if the deterministic stability margin-based assessment is used only, the potential risk of losing system stability caused by wind farm injection uncertainties cannot be revealed.

Furthermore, the standard deviation of wind power for the 31st line

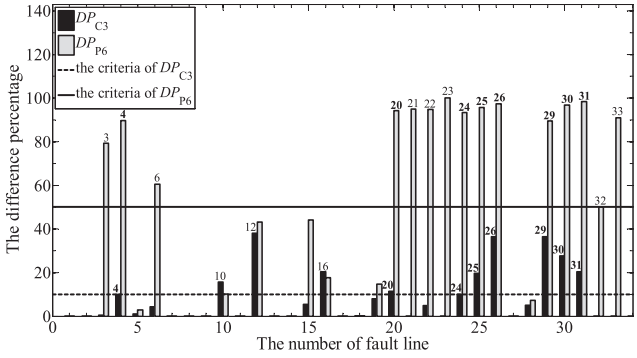

Fig. 23. The values and criteria of *DPn* C3 and *DPn* P6.

in Case C2 is increased by 20–40% (see Fig. 16). Comparing the result in Fig. 16 with Fig. 15, the distance of the nominal operating point to the boundary of PDSR, i.e., stability margins, are the same. But the TSP changes from 0.806 to 0.65, a reduction of 19.355%, indicating that the system has a higher probability of being unstable. This shows that the proposed TSP index can assist in revealing the impact of uncertainty on system stability assessment while the traditional stability margin-based approach may fail to do so.

4.4. Influences of CC and level of wind energy penetrations

IEEE 39-bus and GZ systems are used to study the influences of CC and the level of wind energy penetrations on the results. Two wind farms with different capacities are installed in nodes 33 and 34 on the IEEE 39-bus system and GPTg1 and SLg4 on GZ power system, as shown in Table 14 and Table 15, respectively. Other parameters are the same as Section 4.1.1.

Two indexes, namely the difference percentage (DP) and the average difference percentage (ADP), are introduced to provide more insightful information:

$$DP_i^n = \left| \frac{TSP_i^n - TSP_{\text{ref}}^n}{TSP_{\text{ref}}^n} \right| \times 100\% \tag{28}$$

$$ADP_i = \frac{1}{N} \sum_{n=1}^{N} DP_i^n \tag{29}$$

where $n = 1, 2, \cdots, N$; N is the number of the fault; i represents the number of the case; *TSPn i* and *TSPn* ref are the TSP of fault n under case i and the reference case, respectively.

Case C1 with CC = 0 is taken as the reference and the calculated $ADP_{C2\text{-}C5}$ for different penetration levels of wind power on two different systems are shown in Figs. 17 and 18, respectively. It can be found that the CC has a larger impact on the transient stability results with a higher penetration level of renewable energy. For example, ADP_{C3} and ADP_{C5} with the penetration level 60% is 100 times and 26 times larger than that of the ADP_{C3} and ADP_{C5} with the penetration level 10% on IEEE 39-bus system. ADP_{C3} and ADP_{C5} in Case L3 are 42 and 34 times larger than that of the ADP_{C3} and ADP_{C5} in Case L1 on GZ system.

On the other hand, Figs. 19 and 20 show the impacts of the penetration level of wind power given certain CC. The degree of the shadow color represents the value of TSP. It is observed that for most fault lines, the higher penetration level of wind power is, the smaller TSP is. To provide more details, the values of $ADP_{P2\text{-}P6}$ (reference case is P1) and $ADP_{L2\text{-}L3}$ (reference case is L1) with five different CCs are shown in Figs. 21 and 22. It is clear that given the CC, the higher penetration level of wind power is, the bigger the ADP is. Furthermore, the difference between any two *ADP* remains almost the same as the change of CC.

Table 19
Selected lines with higher DP than the criteria.

	The criterion of DP_{C3} is 10%	The criterion of DP_{P6} is 50%
The chosen fault lines	4, 10, 12, 16, 20, 24, 25, 26, 29, 30, 31	3, 4, 6, 20, 21, 22, 23, 24, 25, 26, 29, 30, 31, 32, 33

4.5. Identification of critical lines

From the above analysis, we conclude that the impacts of the penetration level of wind power and CC vary for different fault lines. This allows us to leverage TSP and DP for the identification of critical lines. Taking the cases in Section 4.1.1 for example, the critical lines that have small TSP values, are listed in Table 16. Furthermore, if the penetration level of wind power is given, the line with the highest DP reveals that it is most sensitive to the CC. By contrast, if the CC is given, the line with the highest DP reveals that it is most sensitive to the penetration level. These results are demonstrated in Table 17 and Table 18, respectively. In particular, the most sensitive lines are the 12th line and the 23rd line, respectively.

On the other hand, depending on the intentions/control purpose of the operator, the sensitive lines can be determined by setting a different criterion for DP. For example, the DP_{C3} with the penetration level being 60%, DP_{P6} with the CC being 0.5 for all lines are listed in Fig. 23. If the criteria for DP_{C3} and DP_{P6} are set as 10% (dotted line) and 50% (solid line), respectively, the lines that have higher DP than the criteria can be chosen as shown in Table 19, where the 4th, 20th, 24th, 25th, 26th, 29th, 30th, and 31st lines belong to both groups.

5. Conclusion and future work

In this paper, a probabilistic transient stability assessment method is proposed considering wind farm uncertainties and correlations. It contains two key steps, namely the derivation of the analytical expression of probabilistic transient stability assessment index based on dynamic security region and the inverse Nataf transformation based three-point estimation and Cornish-Fisher expansion to deal with the uncertainties as well as the correlations among different wind farms. New indices for the identification of critical lines have also been developed. Extensive simulation results carried out on the IEEE test systems and practical GZ system in China show that the computational efficiency of the proposed method is much higher than the Monte Carlo-based method and other methods without the loss of accuracy. In addition, it is found that the CC and the penetration level of wind farms have great impacts on the transient stability of the system. In particular, the higher the penetration level of wind is, the higher probability of transient unstable the system is. Furthermore, the change of CC can significantly influence the TSP under higher penetration level.

The estimated region is dependent on the types of faults and hyperplane coefficients of PDSR are different in different fault cases. However, for a given fault, the dynamic security region is unique and does not vary with operation states. The fault type has been assumed to be known in this paper. This is reasonable as the DSA typically considers the most probable and high-consequence faults according to operational experiences. Future work will be on extending the developed method to deal with the situation when faults are not entirely known while considering wind power uncertainties and correlations.

Declaration of Competing Interest

The authors declare that they have no known competing financial interests or personal relationships that could have appeared to influence the work reported in this paper.

Acknowledgements

This work was supported by the National Basic Research Program of China (“973” Project) (Grant No. 2013CB228204), the National Natural Science Foundation of China (Grant No. 51407126), and Tianjin Natural Science Foundation (Grant No. 15JCQNJC07000).

Appendix A. Supplementary material

Supplementary data to this article can be found online at https://doi.org/10.1016/j.ijepes.2019.105649.

References

[1] Wind Energy Handbook. John Wiley & Sons Ltd. Chichester: West Sussex, UK; 2001. p. 12–39.
[2] Sawyer S, Dyrholm M. Global wind report: annual market update. India: Global Wind Energy Council; 2017.
[3] Morales JM, Conejo AJ, Minguez R. A methodology to generate statistically dependent wind speed scenarios. Appl Energy 2010;87(3):843–55.
[4] Qin ZL, et al. Incorporating multiple correlations among wind speeds, photovoltaic powers and bus loads in composite system reliability evaluation. Appl Energy Oct. 2013;110:285–94.
[5] Song ZF, et al. Assessing transient response of DFIG based wind turbines during voltage dips regarding main flux saturation and rotor deep-bar effect. Appl Energy 2010;87(10):3283–93.
[6] Lojowska A, Kurowickka D, Papaefthymiou G. Stochastic modeling of power demand due to EVS using copula. IEEE Trans Power Syst. 2012;27(4):1960–8.
[7] Kundur P. System protection. Power system stability and control. New York: McGraw-Hill Inc; 1994. p. 17–8.
[8] Odun-Ayo T, Crow ML. Structure-Preserved power system transient stability using stochastic energy functions. IEEE Trans Power Syst 2012;27(3):1450–8.
[9] Hsu YY, Chang CL. Probabilistic transient stability studies using the conditional probability approach. IEEE Trans Power Syst 1988;3(4):1565–72.
[10] Ayodele TR, et al. The impact of wind power on power system transient stability based on probabilistic weighting method. J Renew Sustain Energy 2012;4(6):1469–76.
[11] Faried SO, Billinton R, Aboreshaid S. Probabilistic evaluation of transient stability of a wind farm. IEEE Trans Energy Convers 2009;24(3):733–9.
[12] Anderson P, Bose A. A probabilistic approach to power system stability analysis. IEEE Trans Power Syst 1983;102(8):2430–9.
[13] Ahmadi H, Ghasemi H. Maximum penetration level of wind generation considering power system security limits. IET Gener Transm Distrib 2012;6(11):1164–70.
[14] Chen SK, Shi LB. Transient stability assessment of power system incorporating wind power using Quasi-Monte Carlo method. In: IEEE Region 10 Conf., Macao, China; 2015. p. 1–4.
[15] Vaahedi E, Li W, Chia T, Dommel H. Large scale probabilistic transient stability assessment using B.C. Hydro’s on-line tool. IEEE Trans Power Syst 2000;15(2):661–7.
[16] Han H, Gao S, Shi Q, Cui H, Li F. Security-based active demand response strategy considering uncertainties in power systems. IEEE Access 2017;5:16953–62.
[17] Billinton R, Kuruganty PRS. Probabilistic assessment of transient stability in a practical multi-machine system. IEEE Trans Power Syst 1981;100(7):3634–41.
[18] Preece R, Milanovíc JV. Assessing the applicability of uncertainty importance measures for power system studies. IEEE Trans Power Syst 2016;31(3):2076–84.
[19] Hua KQ, et al. Fast unscented transformation-based transient stability margin estimation incorporating uncertainty of wind generation. IEEE Trans Sustain Energy 2015;6(4):1254–62.
[20] Liu CX, Sun K, Rather ZH, Chen Z, Bak CL, Thøgersen P, et al. A systematic approach for dynamic security assessment and the corresponding preventive control scheme based on decision trees. IEEE Trans Power Syst 2014;29(2):717–30.
[21] Fang JK, Yao W, Wen JY, Cheng SJ, Tang YJ, Cheng Z. Probabilistic assessment of power system transient stability incorporating SMES. Physica C 2013;484(Jan.):276–81.
[22] Zheng C, Malbasa V, Kezunovic M. Regression tree for stability margin prediction using synchrophasor measurements. IEEE Trans Power Syst 2013;28(2):1978–87.
[23] Papadopoulos PN, Milanovic JV. Probabilistic framework for transient stability assessment of power systems with high penetration of renewable generation. IEEE Trans Power Syst 2017;32(4):3078–88.
[24] Xia SW, Luo X, Zhou M, Li GY. Probabilistic transient stability constrained optimal power flow for power systems with multiple correlated uncertain wind generations. IEEE Trans Sustain Energy 2016;7(3):1133–44.
[25] Lu Y, Liang J, Yan JF, Yu ZH, Sun SM, Lu GM, et al. Int. Conf. Power Syst. Tech.

Chengdu, China 2014;2014:2635–41.
[26] Yu YX, Feng F. Active power steady-state security region of power system. Sci China: Series A 1990;33(12):1488–500.
[27] Yu YX. Review of study on methodology of security regions of power system. J Tianjin Univ 2008;41(6):635–46.
[28] Yu YX, Zeng Y. A practical direct method for determining dynamic security regions of electrical power systems. In: Int. Conf. Power Syst. Tech., Kunming, China; 2002. p. 1270–4.
[29] Qin C, Liu YL, Yu YX. Dynamic security region of power systems with double fed induction generator. Trans China-Electr Soc 2015;30(18):157–63.
[30] Liu YL, Yu YX. Transient stability probability of a power system incorporating a wind farm. Sci China-Technol Sci 2016;59(6):973–9.
[31] Morales JM, Baringo L, Conejo AJ, Mínguez R. Probabilistic power flow with correlated wind sources. IET Gener Transm Distrib 2010;4(5):641–51.
[32] Ren ZY, Li WY, Billinton R, Yan W. Probabilistic power flow analysis based on the stochastic response surface method. IEEE Trans Power Syst 2016;31(3):2307–15.
[33] Chang TP. Estimation of wind energy potential using different probability density functions. Appl Energy 2011;88(5):1848–56.
[34] Chang TP. Performance comparison of six numerical methods in estimating Weibull parameters for wind energy application. Appl Energy 2011;88(5):272–82.
[35] Hatziagryriou ND, Karakatsanis TS, Papadopoulos M. Probabilistic load flow in distribution systems containing dispersed wind power generation. IEEE Trans Power Syst 1993;8(1):159–65.
[36] Villanueva D, Pazos JL, Feijóo A. Probabilistic load flow including wind power generation. IEEE Trans Power Syst 2011;26(3):1659–67.
[37] Wang SX, et al. Uncertainty tracing of distributed generations via complex affine arithmetic based unbalanced three-phase power flow. IEEE Trans Power Syst 2015;30(6):3053–62.
[38] Dong C, Yu YX. PDSR in phase angle space and SPM based security monitoring of power systems. In: IEEE Region 10 Conf. (TENCON 2005), Melbourne, Australia; 2005. p. 1–5.
[39] Liu YL, Yu YX. Probabilistic steady-state and dynamic security assessment of power transmission system. Sci China-Technol Sci 2013;56(5):1198–207.
[40] Chen Y, Wen JY, Cheng SJ. Probabilistic load flow method based on Nataf transformation and Latin hypercube sampling. IEEE Trans Sustain Energy 2013;4(2):294–301.
[41] Aien M, et al. Probabilistic optimal power flow in correlated hybrid wind-PV power systems: a review and a new approach. Renew Sust Energ Rev 2015;41(Jan.):1437–46.